HHS Public Access

Author manuscript

*Nat Med*. Author manuscript; available in PMC 2013 December 01.

Published in final edited form as:

*Nat Med*. 2013 June ; 19(6): 704–712. doi:10.1038/nm.3143.

# Inhibition of TGF–β signaling in subchondral bone mesenchymal stem cells attenuates osteoarthritis

**Gehua Zhen**[1,2], **Chunyi Wen**[6,7], **Xiaofeng Jia**[3], **Yu Li**[8], **Janet L. Crane**[1,2], **Simon C. Mears**[1], **Frederic B. Askin**[4], **Frank J. Frassica**[1], **Weizhong Chang**[1,2], **Jie Yao**[6], **Tariq Nayfeh**[1], **Carl Johnson**[1], **Dmitri Artemov**[5], **Qianming Chen**[8], **Zhihe Zhao**[8], **Xuedong Zhou**[8], **Andrew Cosgarea**[1], **John Carrino**[5], **Lee Riley**[1], **Paul Sponseller**[1], **Mei Wan**[1,2], **William Weijia Lu**[6,7], and **Xu Cao**[1,2,*]

[1]Department of Orthopaedic Surgery, School of Medicine, Johns Hopkins University, Baltimore, MD

[2]Institute of Cell Engineering, School of Medicine, Johns Hopkins University, Baltimore, MD

[3]Department of Biomedical Engineering, School of Medicine, Johns Hopkins University, Baltimore, MD

[4]Department of Pathology, School of Medicine, Johns Hopkins University, Baltimore, MD

[5]Department of Radiology and Radiological Science, School of Medicine, Johns Hopkins University, Baltimore, MD

[6]Department of Orthopaedics and Traumatology, Li Ka Shing Faculty of Medicine, The University of Hong Kong, Pokfulam, HKSAR

[7]Center for Human Tissues and Organs Degeneration, Shenzhen Institute of Advanced Technology, Chinese Academy of Science, PR China

[8]State Key Laboratory of Oral Diseases, West China Hospital of Stomatology, Sichuan University; Chengdu, Sichuan 610041, PR China

## Abstract

Osteoarthritis is a highly prevalent and debilitating joint disorder. There is no effective medical therapy for osteoarthritis due to limited understanding of osteoarthritis pathogenesis. We show that TGF–β1 is activated in the subchondral bone in response to altered mechanical loading in an anterior cruciate ligament transection (ACLT) osteoarthritis mouse model. TGF–β1 concentrations



*Correspondence to: Xu Cao, Ross Building, Room 231, 720 Rutland Avenue, Baltimore, MD 21205, Telephone: (410) 502-6440, Fax: (410) 502-6239, xcao11@jhmi.edu.

**Author Contributions:**

G. Z conducted the majority of the experiments, analyzed data and prepared the manuscript. C. W conducted some of the surgery, performed MRI and μCT analysis and helped with manuscript preparation. X. J helped with behavior analysis. Y. L conduced cell culture, Western blot and behavior analysis and helped with manuscript preparation. J. C, W. C, M. W helped with composing manuscript. S. M, F. A, F. F, T. N, C. J, A. C, and P, S provided human specimens. D. A, and J. C helped with MRI analysis. J. Y performed computerized simulation. Q. C, X. Z, L. R, Z. Z, W. L provided suggestions for the project. X. C supervised the project, conceived the experiments and wrote most of the manuscript.

also increased in human osteoarthritis subchondral bone. High concentrations of TGF–β1 induced formation of nestin$^+$ mesenchymal stem cell (MSC) clusters leading to aberrant bone formation accompanied by increased angiogenesis. Transgenic expression of active TGF–β1 in osteoblastic cells induced osteoarthritis. Inhibition of TGF–β activity in subchondral bone attenuated degeneration of osteoarthritis articular cartilage. Notably, knockout of the TGF–β type II receptor (TβRII) in nestin$^+$ MSCs reduced development of osteoarthritis in ACLT mice. Thus, high concentrations of active TGF–β1 in the subchondral bone initiated the pathological changes of osteoarthritis, inhibition of which could be a potential therapeutic approach.

## Introduction

Osteoarthritis is the most common degenerative joint disorder, mainly afflicting the weight–bearing joints, like hips and knees, and is the leading cause of physical disability, predicted to affect 67 million people in the United States by 2030[1]. Despite the identified risk factors, e.g. mechanical, metabolic or genetic, the exact pathogenesis of osteoarthritis remains unclear[2]. Currently, there is no effective disease modifying treatment for osteoarthritis until the end stage of disease necessitating joint replacement[3,4].

Articular cartilage degeneration is the primary concern in osteoarthritis, which has recently been attributed to hypoxia–inducible factor–2α (HIF–2α)[5,6] and complement component 5 (C5)[7], in addition to the well established ADAMTS5[8] and matrix metalloproteinase 13 (MMP13)[9]. Homeostasis and integrity of articular cartilage rely on its biochemical and biomechanical interplay with subchondral bone and other joint tissues[10]. Subchondral bone provides the mechanical support for overlying articular cartilage during the movement of joints and undergoes constant adaptation in response to changes in the mechanical environment through modeling or remodeling[11]. In the situation of instability of mechanical loading on weight bearing joints, such as occurs with ligament injury, excessive body weight, or weakening muscles during aging, the subchondral bone and calcified cartilage zone undergo changes[12]. For instance, rupture of anterior cruciate ligament (ACL) increases the risk of knee osteoarthritis[13], and approximately 20–35% of individuals with osteoarthritis are estimated to have had an incidental ACL tear[14,15]. Clinically, osteophyte formation, subchondral bone sclerosis, disruption of tidemark accompanied by angiogenesis at the osteochondral junction, and articular cartilage degeneration are characteristics of osteoarthritis[16]. Bone marrow lesions are closely associated with pain and implicated to predict the severity of cartilage damage in osteoarthritis[17]. In healthy articular cartilage, matrix turnover remains at relatively low rates and chondrocytes resist proliferation and terminal differentiation[18]. During progression of osteoarthritis, type X collagen, alkaline phosphatase, Runt–related transcription factor 2 (RUNX2), and MMP13 are expressed in articular chondrocytes with decreased proteoglycans and expanded calcified cartilage zones in articular cartilage[2,19]. However, the exact mechanism underlying the potential contributions of subchondral bone to articular cartilage degeneration during osteoarthritis progression is largely unknown.

The role of TGF–β in the pathogenesis of osteoarthritis has drawn more and more attention in recent years. TGF–β is essential for maintenance of articular cartilage metabolic

homeostasis and structural integrity[20]. TGF–β1 stimulates chondrocyte proliferation, and knockout of TGF–β1 or interruption of TGF–β signaling in the articular cartilage results in loss of proteoglycans and cartilage degeneration in mice[21,22]. The elevated ALK1–Smad1/5 vs. ALK5–Smad2/3 ratio in articular cartilage might contribute to pathogenesis of osteoarthritis[23–25]. Several groups have demonstrated that ablation of endogenous TGF–β1 activity reduces osteophyte formation *in vivo* but aggravates articular cartilage degeneration in osteoarthritis animal models[26,27]. We have previously shown that TGF–β1 is activated during osteoclastic bone resorption and induces the migration of bone marrow MSCs to resorption pits for new bone formation serving as a coupling factor[28]. In this study, we investigated the role of TGF–β1 on subchondral bone pathology and articular cartilage degeneration during progression of osteoarthritis. We found that inhibition of TGF–β1 activity in the subchondral bone attenuated its pathological changes and reduced degeneration of articular cartilage in different osteoarthritis animal models.

## Results

### Elevated active TGF-β and bone resorption in subchondral bone

To examine the subchondral bone changes at the onset of osteoarthritis, we transected the ACL in mice to generate a destabilized osteoarthritis animal model and analyzed the effects over time. The tibial subchondral bone volume in ACLT mice dramatically changed relative to sham operated controls post surgery in three–dimensional μCT analysis (Fig. 1a **(top)**). The total subchondral bone tissue volume (TV) increased by more than 20% compared to that of sham controls by 2 months post surgery (Fig. 1b). The thickness of subchondral bone plate (SBP) fluctuated significantly from 14 to 60 days post surgery with abnormal morphology by 60 days (Fig. 1c). Moreover, the disruption of connectivity and micro–architecture of trabecular bone was indicated by significantly increased trabecular pattern factor (Tb. Pf)[29] in the ACLT mice compared to that of sham operated controls (Fig. 1d), indicating uncoupled bone remodeling. Proteoglycan loss in cartilage was observed 30 days post surgery and was further aggravated at 60 days (Fig. 1a **(center)**). Notably, proteoglycan loss was detected at the deep zone of articular cartilage (arrows). H&E staining showed that thickness of the calcified cartilage zone increased with the tidemark moving closer to articular surface. (Fig. 1a **(bottom)**, double arrowed lines). OARSI scores[30] revealed the degeneration of articular cartilage started by 14 days post ACLT and progressed gradually (Fig. 1e). TRAP staining showed that the number of osteoclasts increased in the subchondral bone as early as 7 days post surgery, and the continued osteoclastic bone resorption generated large bone marrow cavities by 30 days (Fig. 1f **(top)** and **a (top)**). Immunostaining demonstrated that post surgery, the number of pSmad2/3$^+$ cells increased by 7 days, maintained at high concentrations until 30 days and then gradually decreased back to baseline by 60 days (Fig. 1f **(bottom)**). The results suggest that altered mechanical loading induced subchondral bone resorption with elevated TGF–β concentrations in the subchondral bone.

### Expression of active TGF–β1 in bone induces osteoarthritis

In Camurati Engelmann disease (CED), TGF–β1 is activated upon secretion due to a point activating mutation in the *TGFB1* gene[28,31], and interestingly, people with CED are prone to

develop osteoarthritis[20,32]. To examine whether high concentrations of active TGF–β1 in the subchondral bone initiates osteoarthritis, we used a CED activation mutation mouse model in which TGF–β1 is activated upon secretion in the subchondral bone marrow by osteoblastic cells. Three–dimensional μCT images of cross sectional, coronal and sagittal views of tibial subchondral bone showed uneven distribution of bone mass in CED mice relative to their wild type littermates, indicating disrupted bone formation (Fig. 2a). Similar to the ACLT mouse model, the tibial subchondral bone TV and Tb.Pf increased whereas thickness of the SBP decreased in CED mice relative to their wild–type littermates. Notably, significant proteoglycan loss was detected at the calcified cartilage zone adjacent to the subchondral plate (Fig. 2b **(top)**). The thickness of calcified cartilage layer significantly increased whereas the hyaline cartilage layer decreased with apparent hypocellularity (Fig. 2b **(bottom)**). The OARSI scores revealed significant degeneration of articular cartilage in CED mice relative to their age matched littermates (Fig. 2c).

We also measured angiogenesis in these mice using microfil contrast enhanced angiography since it is a pathological manifestation of osteoarthritis[33]. The volume fraction and number of blood vessels in subchondral bone increased significantly in CED mice relative to their wild–type littermates (Fig. 2d). Consistently, the number of $CD31^+$ endothelial progenitor cells also increased (Fig. 2e). Immunostaining for nestin, primarily expressed in adult bone marrow MSCs[34,35], revealed a significantly higher number of $nestin^+$ cells in the subchondral bone marrow of CED mice compared to wild type controls (Fig. 2f). Once committed to the osteoblast lineage, MSCs express osterix, a marker of osteoprogenitors. The number of $osterix^+$ osteoprogenitors also significantly increased in the subchondral bone marrow compared to wild type controls (Fig. 2f), indicating $nestin^+$ MSCs undergo osteoblastic differentiation for de novo bone formation. In addition, we also measured active TGF–β1 in the subchondral bone of human knee joints at different stages of osteoarthritis. ELISA analysis showed that the concentrations of active TGF–β1 in the subchondral bone of human osteoarthritis knee joints were significantly higher than those of healthy controls (Fig. 2g). Collectively, development of the knee joint osteoarthritis phenotype in CED mice was similar to that observed in the ACLT mouse model, revealing that high concentrations of active TGF–β1–induced abnormal subchondral bone formation may contribute to the degeneration of articular cartilage.

## Subchondral bone TGF–β inhibition attenuates cartilage degeneration

We next examined the effects of inhibition of TGF–β activity on ACLT joints. Injection of TβRI inhibitor (SB505124) has been shown to rescue uncoupled bone formation induced by high concentrations of active TGF–β1[28]. We screened different doses of the TβRI inhibitor with ACLT mice to identify the optimal dose (Supplementary Fig. 3). Low concentrations of TβRI inhibitor (0.1 or 0.5 mg $kg^{-1}$) had minimal effects on the subchondral bone, whereas higher concentrations, beginning at 1 mg $kg^{-1}$improved subchondral bone structure (Fig. 3a). On the contrary, proteoglycan loss in articular cartilage was induced at higher concentrations (2.5 or 5 mg $kg^{-1}$) (Supplementary Fig. 3a). Of note, proteoglycan loss induced by higher doses of inhibitor was primarily observed in the superficial to middle zones of articular cartilage (Supplementary Fig. 3a). Improvement of trabeculae connectivity and micro–architecture with 1 mg $kg^{-1}$ of the TβRI inhibitor was demonstrated by

normalization of subchondral bone TV (Fig. 3b), maintenance of the thickness of SBP (Fig. 3c) and volume decrease in Tb. Pf (Fig. 3d). Notably, proteoglycan loss and calcification of articular cartilage were attenuated in ACLT mice 2 months post surgery, a time point often used for analysis of destabilized osteoarthritis mice models[36] (Fig. 3e). The protective effect of the TβRI inhibitor on articular cartilage in TβRI inhibitor treated compared to vehicle treated ACLT mice was quantified using OARSI system (Fig. 3f). The inhibitor had no significant effects on the elevated concentrations of MMP13 or type X collagen in chondrocytes as compared to vehicle treated ACLT group (Fig. 3g, h).

Similar results were observed in 9–month–old ACLT mice. Subchondral bone structure was improved and articular cartilage degeneration was attenuated in aged ACLT mice treated with 1 mg $kg^{-1}$ of TβRI inhibitor (Supplementary Fig. 6). Moreover, gait analysis with Catwalk system revealed significant disparity between the percentages of maximum contact time (Maxcontactat%) of the two hind limbs two months post surgery, which was rescued in the inhibitor–treated ACLT group (Fig. 3i). Taken together, the results indicate that TGF–β plays distinct roles in the subchondral bone and articular cartilage and inhibition of TGF–β activity in the subchondral bone may prevent degeneration of articular cartilage during osteoarthritis development.

## Increase of MSCs leads to aberrant bone remodeling

To examine the cellular mechanism, we analyzed the effect of TβRI inhibitor on MSCs in the subchondral bone. We found by immunostaining that $nestin^+$ MSCs in subchondral bone marrow were dramatically increased in numbers by 30 days post surgery in ACLT mice as compared to that of sham controls (Fig. 4a). This effect was prevented by the TβRI inhibitor (Fig. 4a). Similarly, $osterix^+$ osteoprogenitors were largely located on the bone surface in sham controls (Fig. 4a) and the significantly increased number of osteoprogenitor clusters detected in the bone marrow in the vehicle–treated ACLT group was attenuated with TβRI inhibitor treatment (Fig. 4a). These results were confirmed in flow cytometry analysis of $nestin^+$ MSCs and $osterix^+$ osteoprogenitors from subchondral bone (Fig. 4c). $Osteocalcin^+$ osteoblasts and osteoids were observed in the marrow of the ACLT subchondral bone. Injection of TβRI inhibitor reduced the abnormal localization, as the $osteocalcin^+$ osteoblasts and osteoid were largely found on the bone surface, similar to their location in sham controls (Fig. 4b). Uncoupled bone remodeling was rescued by the TβRI inhibitor compared to the vehicle–treated group in fluorescent double labeling experiment (Fig. 4d).

Phosphorylation of Smad1 can be activated by TGF–β1 in endothelial progenitor cells[37]. We examined whether TGF–β1 activates phosphorylation of Smad1 in MSCs. We found that TGF–β1 stimulated phosphorylation of both Smad2/3 and Smad1/5/8 at low concentrations, but a maximal increase of phosphorylated Smad1/5/8 was achieved at a higher dose of TGF–β1 (5 ng $ml^{-1}$) (Fig. 4e). Immunostaining of the subchondral bone showed that the number of $pSmad1^+$ cells remained relatively stable in ACLT mice treated with TβRI inhibitor relative to sham controls. (Fig. 4f). In contrast, $pSmad2/3^+$ cells were greatly increased in ACLT mice and the increase was prevented by TβRI inhibitor treatment (Fig. 4f), suggesting that phosphorylation of Smad2/3 is the primary downstream signal of TGF–β in the subchondral bone MSCs. Consistently, the expression level of ALK1 remained

unchanged in ACLT mice treated with vehicle or inhibitor relative to sham operated control mice whereas the expression of ALK5 was significantly increased in ACLT mice relative to control mice and the increase was inhibited with injection of TβRI inhibitor (Fig. 4f). $CD31^+$ endothelial progenitors were significantly increased in the subchondral bone of ACLT mice relative to sham controls, which was reduced by injection of TβRI inhibitor. (Fig. 4g). Microfil contrast–enhanced angiography of subchondral bone confirmed that the inhibitor decreased angiogenesis (Fig. 4h). The contrast signal was significantly increased in vehicle treated mice at 1 month post ACLT in MRI perfusion analysis and the increase was prevented in the inhibitor treated group, indicating reduced new vessel formation (Fig. 4i). The bone marrow lesion in tibial subchondral bone detected by micro–MRI was also obviously smaller in size in the ACLT- inhibitor treated mice as compared to that of ACLT-vehicle treated mice (Fig. 4j). These results indicate that high concentrations of active TGF–β increased the number of $nestin^+$ MSCs, leading to aberrant subchondral bone formation and angiogenesis, representing pathological changes of subchondral bone post ACLT.

## Neutralizing subchondral TGF–β reduces osteoarthritic severity

To validate the role of TGF–β in the subchondral bone at the onset of osteoarthritis, we implanted TGF–β antibody (1D11)[38,39] in alginate beads[40,41] directly in the tibial subchondral bone of rat ACLT joints. The knee joints were harvested 3 months post surgery. Similar to systemic use of TβRI inhibitor, the micro–architecture of the bone was improved with local application of the antibody as compared to that of vehicle–treated ACLT rats (Fig. 5a–d). The number of $osterix^+$ progenitor clusters in bone marrow cavity of rat ACLT joints was significantly less in antibody treated rats compared to that of the vehicle–treated rats (Fig. 5e). Notably, degeneration of articular cartilage was attenuated as reflected in OARSI scores by administration of the antibody in the subchondral bone (Fig. 5f **(top), g**). Moreover, the percentages of $MMP13^+$ and type X $collagen^+$ chondrocytes were significantly reduced, indicating protection from degeneration of articular cartilage (Fig. 5f). In contrast, MMP13 and ColX expression were not reduced significantly with systemic injection of TβRI inhibitor (Fig. 3g, h) since TGF–β is essential for homeostasis of articular cartilage. Therefore, specific administration of TGF–β antibody in the subchonbdral bone reduced aberrant bone formation, but did not inhibit TGF–β signaling in articular cartilage. The protective effect on articular cartilage in our rat osteoarthritis model was primarily through improvement of subchondral bone by site–specific administration of TGF–β antibody. The results further validate that the role of TGF–β in the subchondral bone is distinct from its role in articular cartilage; high concentrations of active TGF–β1 in the subchondral bone induced abnormal bone formation leading to development of osteoarthritis.

## Knockout of *TGFBR2* in MSCs reduces osteoarthritic severity

TGF–β binds to a complex of TGF–β type II receptor (TβRII) and TβRI to induce phosphorylation of downstream Smad2/3. Deletion of the *TGFBR2* ensures blocking of the TGF–β signaling cascade. We induced knockout of *TGFBR2* in $nestin^+$ MSCs of ACLT mice to confirm the critical role of TGF–β signaling in MSCs at the onset of osteoarthritis. *Nestin–Cre*$^{TM}$*ER::TβRII*$^{fl/fl}$ mice were injected with tamoxifen to delete *TGFBR2* (*TβRII*$^{-/-}$) in the nestin MSCs unresponsive to TGF–β while the TGF–β signaling pathway in other cell

types, including chondrocytes remained intact (Supplementary Fig. 7). Similar to those of TβRI inhibitor treatment, the micro–architecture and Tb. Pf were significantly improved in the ACLT *TβRII*$^{-/-}$mice at 2 months post surgery relative to the ACLT wild type littermates (Fig. 6a). Osterix$^{+}$ osteoprogenitors in the subchondral bone remained primarily on the bone surface similar to ACLT wild type littermates (Fig. 6b). Moreover, co–staining of β–gal and osteocalcin in the subchondral bone of *Nestin–Cre*$^{TM}$*ER:: Rosa26 LacZ*$^{fl/fl}$ mice revealed that the β–gal$^{+}$ MSC lineage cells were detected in the bone marrow in the vehicle–treated ACLT mice whereas β–gal$^{+}$ cells were primarily distributed on bone surface and were osteocalcin$^{+}$ in sham controls and TβRI inhibitor treated ACLT mice (Fig. 6c). The proteoglycan loss in articular cartilage was reduced in the ACLT *TβRII*$^{-/-}$ mice (Fig. 6d **(top)**). Calcification of articular cartilage was also attenuated and the thickness of calcified cartilage remained unchanged relative to ACLT wild type mice (Fig. 6d **(bottom)**). Immunostaining demonstrated that the concentrations of MMP13 and type X collagen expression were significantly inhibited in ACLT *TβRII*$^{-/-}$ mice relative to their ACLT wild–type littermates, indicating inhibition of articular cartilage degeneration (Fig. 6g). The protective effects on articular cartilage in ACLT *TβRII*$^{-/-}$ mice were reflected in OARSI scores (Fig. 6e). The disparity between the percentage of maximum contact time (Maxcontactat%) of the two hind limbs in wild type ACLT mice did not occur in their ACLT *TβRII* $^{-/-}$littermates as revealed by gait analysis (Fig. 6f). Thus, this data further demonstrates that high concentrations of TGF–β initiates pathological changes in subchondral bone MSCs, contributing to the onset of osteoarthritis.

## Discussion

TGF–β is known for its anabolic effects on articular cartilage homeostasis by stimulating the production of extracellular matrix proteins and preventing terminal differentiation of chondrocytes[42,43]. In this study, we found that changes in mechanical loading on the joints increased the number of osteoclasts in the subchondral bone as early as 7 days post surgery in the ACLT animal model. High concentrations of TGF–β1 were activated during osteoclast bone resorption to recruit nestin$^{+}$ MSCs for the subsequent uncoupled bone formation. Notably, osteoclastic bone resorption was spatiotemporally uncoupled with TGF–β1–induced recruitment of nestin$^{+}$ MSCs and led to abberant bone formation, which was further substantiated by development of osteoarthritic–like changes in CED mice. Relative to a single phase of uncoupled sequential bone resorption and formation in the mouse ACLT model, human osteoarthritis appeared more complex with multiple phases. We found some areas of the articular cartilage were still intact or in the middle stage of osteoarthritis progression when analyzing specimens from late stage osteoarthritis subjects who underwent knee joint replacement. Consistently, the thickness of the subchondral plate in osteoarthritis specimens is not uniform, although the percent distribution of subchondral plate generally became thicker (Supplementary Fig. 1). Moreover, the concentrations of active TGF–β were higher in subchondral bone with articular cartilage compared that of the healthy controls. The observation suggests that inhibition of TGF–β activity in the subchondral bone may still have therapeutic effects even if individuals with osteoarthritis are not in the early stages. Our findings reveal that TGF–β plays a different role in subchondral bone as opposed to its anabolic effect on articular cartilage. Thus, the location

of the elevated TGF–β1 concentrations in subchondral bone triggers a cascade of events that lead to the development of osteoarthritis.

Both clinical and animal studies report that progression of osteoarthritis is accompanied by the accumulation of mesenchymal progenitor cells in joint tissues and synovial fluids[44,45]. Bone marrow lesions have been identified as a prognostic factor of osteoarthritis progression as it has been found to populate sites of cartilage destruction[16,17,46]. We observed that elevations in TGF–β1 concentrations lead to an increased number of nestin$^+$ MSCs in the subchondral bone marrow in various osteoarthritis animal models. During the normal remodeling process, osteoblasts and their progenitors are primarily observed at the resorption site on the bone surface. However, the altered microenvironment induced by abnormal mechanical loading may lead to “in situ” commitment of osteoprogenitors in the bone marrow cavities. Bone marrow lesions have been characterized as less well mineralized newly formed bone[46]. These clustered bone marrow osteoprogenitors may lead to the de novo bone formation that is visualized as bone marrow lesions under MRI. Moreover, knockout of *TGFBR2* in nestin$^+$ MSCs attenuated the development of osteoarthritis in ACLT mice. This result further confirmed our hypothesis that MSCs are the target cells of the aberrant TGF–β signals during osteoarthritis progression. Additionally, bone formation is often coupled with angiogenesis. It is known that the TGF–β signaling pathway in endothelial progenitor cells can promote angiogenesis[47] and TGF–β may stimulate the paracrine machinery in MSCs that further facilitate angiogenesis[48,49]. Our data revealed that blood vessels were increased in the subchondral bone of both ACLT and CED mice in angiography by microphil–perfused experiments. Reduced angiogenesis by inhibition of TGF–β activity may have further attenuated the de novo bone formation in the subchondral bone in the osteoarthritis joints of ACLT mice.

The subchondral bone and articular cartilage act as a functional unit in the joint[10]. In human osteoarthritis joints, the subchondral plates become significantly thicker relative to that of healthy subjects[51]. The subchondral bone was modeled post surgery in ACLT animal models and their thickness dramatically fluctuated. The capacity of chondrocytes to modulate their functional state in response to alterations in mechanical loading is relatively limited compared to the adjacent subchondral bone. Changes in osteochondral junction are therefore likely involved in advancement of the calcified cartilage zone[50,52,53]. The precise mechanism of degeneration of articular cartilage through abnormal subchondral bone changes is still unclear. In our established simulation model for human knee joints, expansion and increased stiffness of subchondral bone (Supplementary Fig. 8) changed the distribution of articular cartilage stress. Therefore, TGF–β–induced abnormal bone formation may contribute to the alteration of the mechanical property of subchondral bone and initiate its expansion causing degeneration of articular cartilage.

## Methods

### Human Subjects

After IRB approval, we collected tibial plateau specimens from 78 individuals with osteoarthritis that were undergoing total knee replacement surgery. The specimens were

processed for μCT, ELISA and histological examination. We purchased healthy knees specimens from the Nation Disease Research Interchange (NDRI) to serves as controls.

## Animals

### Mice

We purchased C57BL/6J (wild type) mice from Charles River. We anesthetized two months old male mice with ketamine and xylazine and then transected the anterior cruciate ligament surgically to induce mechanical instability associated osteoarthritis on the right knee. Sham operations were done on independent mice. For the time–course experiment, operated animals were euthanized at 0, 14, 30, 60 and 90 days post surgery, $n$ = 8–12. For the dosage screening experiment, 2–month–old sham and ACLT operated mice were assigned into 6 groups, $n$ = 10 per group. Beginning three days after surgery, we injected either different doses (0.1, 0.5, 1, 2.5, and 5 mg $kg^{-1}$) of TβRI inhibitor (SB505124, Sigma Aldrich) or the equivalent volume of vehicle (DMSO+PBS) intra–peritoneally daily for 30 days. Mice were euthanized 30 and 60 days post surgery.

We purchased *Nestin–Cre$^{TM}$ER* and *(ROSA)26Sortm1Sor/J* mice from the Jackson Laboratory. Floxed type II TGF–β receptor (*TβRII$^{fl/fl}$*) mice were obtained from Dr. Moses' lab[54]. *Nestin–Cre$^{TM}$ER* mice were crossed with *TβRII$^{fl/fl}$* mice. The offspring were intercrossed to generate the following offspring: *nestin–Cre$^{TM}$ER:: TβRII$^{fl/fl}$*, in which *Cre* was fused with a mutated estrogen receptor that could be activated by Tamoxifen. We determined the genotype of transgenic mice by PCR analyses of genomic DNA isolated from mouse tails. Genotyping for the Cre transgene was performed by PCR with the primers Cre 5′ (5′–CAAATAGCCCTGGCAGAT–3′) and Cre 3′=e;(5′–TGATACAAGGGACATCTTCC–3′). The *loxP TβRII* allele was identified with the primerslox1F (5′–TAAACAAGGTCCGGAGCCCA–3′) and lox1R (5′–ACTTCTGCAAGAGGTCCCCT–3′)[55]. We generated *Nestin–Cre$^{TM}$ER:: Rosa26–LacZ $^{fl/fl}$* mice by crossing *nestin–Cre$^{TM}$ER* mice with mice homozygous with a loxP–flanked DNA STOP sequence preventing expression of the downstream lacZ gene. The offspring were then intercrossed to generate the following genotype: *Nestin–Cre$^{TM}$ER:: Rosa26–LacZ $^{fl/fl}$*. We performed sham or ACLT operations on two month–old, male WT, *Nestin–Cre$^{TM}$ER:: TβRII$^{fl/fl}$* and *Nestin–Cre$^{TM}$ER:: Rosa26–LacZ $^{fl/fl}$* male mice. Three days after surgery, we treated each group with 100 mg $kg^{-1}$ body weight of tamoxifen daily for 30 days and sacrificed the mice at either 30 or 60 days after surgery ($n$ = 8 per treatment group). CED mice were generated in our laboratory as previously described, in which the CED–derived TGF–β1 mutation (H222D) is specifically expressed by osteoblastic cells driven by a 2.3–kb type I collagen promoter[28].

### Rats

We purchased two month–old male Lewis rats from Charles River. ACLT was conducted as described as above. After ACLT, we made a canal in the medial plateau using a 20G needle. An alginate bead containing 0.1 μg 1D11 (TGF–β1 neutralizing antibody, R&D Systems, Minneapolis, MN) or vehicle was embedded in the subchondral bone canal. The canal was

then closed with bone wax. We euthanized the animals at 0, 1, 2, and 3 months post surgery ($n$ = 8 per group). Knee joints were processed for μCT and histological analysis accordingly.

All animals were maintained in the Animal Facility of the Johns Hopkins University School of Medicine. The experimental protocol was reviewed and approved by the Institutional Animal Care and Use Committee of the Johns Hopkins University, Baltimore, MD, USA.

### Cell Culture

We obtained green fluorescent protein (GFP) labeled mouse adult MSCs from the Texas A&M Health Science Center College of Medicine Institute (College Station). We maintained cells (Passage 3–5) in Iscove's modified Dulbecco's medium (Invitrogen) supplemented with 10% fetal calf serum (Atlanta Biologicals), 10% horse serum (Thermo Scientific), and 1% penicillin–streptomycin (Mediatech). We cultured MSCs in 6 well plates at a density of $1.8 \times 10^5$ cells per well, then starved them for 6 h followed by TGF–β1 (R&D Systems) and TβRI inhibitor (SB–505124) (Sigma–Aldrich) treatment as indicated.

### ELISA and Western blot

We determined the concentration of active TGF–β1 in the conditioned media by the ELISA Development kit (R&D Systems) according to the manufacturer's instructions. Western blot analyses were conducted on the protein of lysates from in vitro cultured MSCs. The cell lysates were centrifuged and the supernatants were separated by SDS–PAGE and blotted on polyvinylidene fluoride membrane (Bio–Rad Laboratories). Following incubation in specific antibodies, we detected proteins using an enhanced chemiluminescence kit (Amersham Biosciences). We used antibodies recognizing mouse pSmad1/5 (Cell Signaling technology Inc., 1:500), pSmad2 (Cell Signaling technology Inc., 1:1000), Smad1/5/8 (Cell Signaling technology Inc., 1:1000) and Smad2 (Cell Signaling technology Inc., 1:1000) to examine the protein concentrations in the lysates.

### Histochemistry, immunohistochemistry and histomorphometry

At the time of sacrifice, we resected and fixed the knee joints in 10% buffered formalin for 48 hours, decalcified in 10% ethylenediamine tetraacetic acid (pH 7.4) for 21 days and embedded in paraffin or O.C.T. compound (Sakura Finetek). Four–μm–thick sagittal oriented sections of the knee joint medial compartment were processed for hematoxylin and eosin and sanfranin O–Fast green staining. Tartrate resistant acid phosphatase staining was performed using standard protocol (Sigma–Aldrich). Immunostaining was performed using standard protocol. We incubated sections with primary antibodies to mouse Nestin (Aves Labs, Inc., 1:300), Osterix (Abcam, 1:600), Osteocalcin (Takara bio Inc., 1:200), p–Smad2/3 (Santa Cruz Biotechnology Inc., 1:50), p–Smad1/5 (Abcam, 1:50), ALK1 (Santa Cruz Biotechnology Inc., 1:50), ALK5 (Abcam, 1:50), CD31 (Abcam, 1:100), MMP13 (Abcam, 1:40), and Collagen X (Abcam, 1:80) overnight at 4°C. For immunohistochemical staining, a horse radish peroxidase–streptavidin detection system (Dako) was subsequently used to detect the immunoactivity followed by counterstaining with hematoxylin (Dako). For immunofluorescent staining, secondary antibodies conjugated with fluorescence were added and slides were incubated at room temperature for 1 hour while avoiding light. We microphotographed sections to perform histomorphometric measurements on the entire area

of the tibia subchondral bone (Olympus DP71). Quantitative histomorphometric analysis was conducted in a blinded fashion with OsteoMeasureXP Software (OsteoMetrics, Inc.). To label mineralization deposition, sequential subcutaneous injections of 1% calcein (Sigma, 15 mg $kg^{-1}$) and 3% xylenol orange (Sigma, 90mg $kg^{-1}$) in 2% sodium bicarbonate solution was performed. Calcein and xylenol orange were injected 10 days and 2 days respectively before the mice were sacrificed. We counted the number of positively stained cells in whole tibia subchondral bone area per specimen, in five sequential sections per mouse in each group. We calculated OARSI scores as previously described[30].

## Flow cytometry

We divided C57/Bl6 mice into 3 groups ($n$ = 10 per group): sham operation with vehicle treatment, ACLT with vehicle treatment and ACLT with TβRI inhibitor (SB505124) treatment. One month after surgery, we sacrificed mice and pooled tibia subchondral bone marrow cells from each group together. Red blood cells were lysed by commercial ACK lysis buffer (Quality Biological, Inc.). After centrifugation, the cell pellet was resuspended and fixed in 4% paraformaldehyde. We then washed cells with 0.1% bovine serum albumin (BSA) in PBS and counted them. $1\times10^6$ cells per milliliter were permeabilized in 0.1% Triton X–100 prior to blocking in 3% FACS buffer (PBS, 3% FBS, 0.1% NaN3 sodium azide) for 30 min on ice. We incubated the cells with Alexa Fluor 647–conjugated Nestin antibody (BD Pharmingen), anti–Osterix (Abcam, 1:400) or isotype control for 1 hour at 37°C in dark room, and then washed twice with 0.1% BSA in PBS. The cells for Osterix staining were further incubated with fluorochrome–conjugatd secondary antibody for 30 minutes on ice. The cells were acquired immediately after washing with 3% FACS buffer. Probes were analyzed using a FACS Calibur flow cytometer and CellQuest software (Becton Dickinson).

## In vivo micro–MRI

We performed all MRI studies on a horizontal 30 cm bore 9.4T Bruker Biospec preclinical scanner, using a custom–built, single–turn volume coil positioned orthogonal to the $B_0$ magnetic field[56,57]. Anesthesia was initiated with 4% isoflurane and maintained with a 2% isoflurane/oxygen mixture. We acquired T2–weighted images with a 2D RARE (Rapid Acquisition with Relaxation Enhancement) sequence, TE/TR (echo time/repetition time) = 15.17/3000 ms, 35 slices at thickness of 0.35 mm, FOV 1.75 × 1.75 cm, and matrix size 256 × 128. We acquired T2–weighted images with a chemical shift selective fat saturation pulse tuned to the fat resonant frequency. All T2–weighted images were processed to a final matrix size of 256 × 256 with an isotropic resolution of 0.068 mm $pixel^{-1}$. We acquired T1–weighted images with a 3D gradient echo sequence using a 30° flip angle, TE/TR = 1.5/8 ms, FOV 1.5 × 1.5 × 1.5 cm, and matrix size 128 × 64 × 64 before and for 10 minutes after the injection of 0.1 ml 0.1M gadopentetate dimeglumine. All T1–weighted images were processed to a final matrix size of 128 × 128 × 128 with an isotropic resolution of 0.12 mm $pixel^{-1}$.

### Micro–computed tomography (μCT)

We dissected knee joints from mice free of soft tissue, fixed overnight in 70% ethanol and analyzed by high resolution μCT (Skyscan1172) [58]. We reconstructed and analyzed images using NRecon v1.6 and CTAn v1.9, respectively. Three–dimensional model visualization software, CTVol v2.0, was used to analyze parameters of the trabecular bone in the metaphysis. The scanner was set at a voltage of 50 kVp, a current of 200 μA and a resolution of 5.7 μm per pixel. Cross–sectional images of the tibiae subchondral bone were used to perform three–dimensional histomorphometric analysis. We defined the region of interest to cover the whole subchondral bone medial compartment, and we used a total of ten consecutive images from medial tibial plateau for 3–D reconstruction and analysis. Three–dimensional structural parameters analyzed included: TV: total tissue volume (contains both trabecular and cortical bone), BV/TV: trabecular bone volume per tissue volume, Tb. Th: trabecular thickness, Tb. Sp: trabecular separation, SMI, Conn. Dn: connectivity density, and Tb.Pf: trabecular pattern factor.

### CT based microangiography

We imaged blood vessels in bone by angiography of microphil–perfused long bones [59]. Briefly, after we euthanized the animals and opened the thoracic cavity, the inferior vena cava was severed. We flushed the vasculat system with 0.9% normal saline solution containing heparin sodium (100 U $mL^{-1}$) through a needle inserted into the left ventricle. The specimens were pressure fixed with 10% neutral buffered formalin. We washed formalin from the vessels by using heparinized saline solution and then injected a radiopaque silicone rubber compound containing lead chromate (Microfil MV–122; Flow Tech) to label the vasculature. Samples were stored at 4 °C overnight for contrast agent polymerization. Mouse femurs were dissected from the specimens and soaked for 4 d in 10% neutral buffered formalin to ensure complete tissue fixation. We treated specimens for 48 h in a formic acid–based solution (Cal–Ex II) to decalcify the bone and facilitate image thresholding of the femoral vasculature from the surrounding tissues. Images were obtained using μCT imaging system (Skyscan 1172) at a resolution of 9–μm isotropic voxel size. A threshold of 60 was initially chosen based on visual interpretation of threshold 2D tomograms.

### Gait Analysis

We performed automated gait analysis pre–surgery and 2, 4, 6 and 8 weeks post–surgery using a “CatWalk” system (Noldus). All experiments were performed during the same period of the day (1:00 PM to 4:00 PM) and analyzed as previously reported[60,61]. Briefly, we trained mice to cross the Catwalk walkway daily for 7 days before ACLT or sham operation. During the test, each mouse was placed individually in the Catwalk walkway, which consists of a glass plate (100×15×0.6 cm) plus two Plexiglas walls, spaced 8 cm apart. The mouse was allowed to walk freely and traverse from one side to the other of the walkway glass plate. Two infrared light beams spaced 90 cm apart were used to detect the arrival of the mouse and to control the start and end of data acquisition. We carried the recordings out when the room was completely dark, with the exception of the light from the computer screen. LED light from an encased fluorescent lamp was emitted inside the glass

plate and completely internally reflected. When the mouse paws made contact with the glass plate, light was reflected down and the illuminated contact area was recorded with a high speed color video camera positioned underneath the glass plate connected to a computer running Catwalk software v9.1 (Noldus). Comparison was made between the ipsilateral (left) and the contralateral (right) hind paw in each run of each animal at each time point. Paired *t*–test was used for statistical analysis.

### Statistics

Data are presented as mean ± standard deviation. The comparisons for OARSI scores, bone mass and microarchitecture among different groups were performed using multiple–factorial analysis of variance (ANOVA). When ANOVA testing indicated overall significance of main effects and without interaction between them, the difference between individual time points and sites was assessed by *post hoc* tests. The level of significance was set at $P < 0.05$. All data analyses were performed using SPSS 15.0 analysis software (SPSS Inc).

## Supplementary Material

Refer to Web version on PubMed Central for supplementary material.

## Acknowledgments

This research was supported by National Institutes of Health Grant DK 057501 (XC), and DK 08098 (XC). Thanks Rachael Luck; Lynne Sakowski for collecting samples.

## References

1. Hootman JM, Helmick CG. Projections of US prevalence of arthritis and associated activity limitations. Arthritis Rheum. 2006; 54:226–229. [PubMed: 16385518]
2. van den Berg WB. Osteoarthritis year 2010 in review: pathomechanisms. Osteoarthritis Cartilage. 2011; 19:338–341. [PubMed: 21324370]
3. Berenbaum F. Osteoarthritis year 2010 in review: pharmacological therapies. Osteoarthritis Cartilage. 2011; 19:361–365. [PubMed: 21320615]
4. Hawker GA, Mian S, Bednis K, Stanaitis I. Osteoarthritis year 2010 in review: non-pharmacologic therapy. Osteoarthritis Cartilage. 2011; 19:366–374. [PubMed: 21324369]
5. Saito T, et al. Transcriptional regulation of endochondral ossification by HIF-2alpha during skeletal growth and osteoarthritis development. Nat Med. 2010; 16:678–686. [PubMed: 20495570]
6. Yang S, et al. Hypoxia-inducible factor-2alpha is a catabolic regulator of osteoarthritic cartilage destruction. Nat Med. 2010; 16:687–693. [PubMed: 20495569]
7. Wang Q, et al. Identification of a central role for complement in osteoarthritis. Nat Med. 2011; 17:1674–1679. [PubMed: 22057346]
8. Glasson SS, et al. Deletion of active ADAMTS5 prevents cartilage degradation in a murine model of osteoarthritis. Nature. 2005; 434:644–648. [PubMed: 15800624]
9. Neuhold LA, et al. Postnatal expression in hyaline cartilage of constitutively active human collagenase-3 (MMP-13) induces osteoarthritis in mice. J Clin Invest. 2001; 107:35–44. [PubMed: 11134178]
10. Lories RJ, Luyten FP. The bone-cartilage unit in osteoarthritis. Nat Rev Rheumatol. 2011; 7:43–49. [PubMed: 21135881]
11. Madry H, van Dijk CN, Mueller-Gerbl M. The basic science of the subchondral bone. Knee Surg Sports Traumatol Arthrosc. 2010; 18:419–433. [PubMed: 20119671]

12. Burr DB, Radin EL. Microfractures and microcracks in subchondral bone: are they relevant to osteoarthrosis? Rheum Dis Clin North Am. 2003; 29:675–685. [PubMed: 14603577]
13. Stein V, et al. Pattern of joint damage in persons with knee osteoarthritis and concomitant ACL tears. Rheumatol Int. 2010; 32:1197–1208. [PubMed: 21253735]
14. Amin S, et al. Complete anterior cruciate ligament tear and the risk for cartilage loss and progression of symptoms in men and women with knee osteoarthritis. Osteoarthritis Cartilage. 2008; 16:897–902. [PubMed: 18203629]
15. Hill CL, et al. Cruciate ligament integrity in osteoarthritis of the knee. Arthritis Rheum. 2005; 52:794–799. [PubMed: 15751064]
16. Suri S, Walsh DA. Osteochondral alterations in osteoarthritis. Bone. 2012; 51:204–211. [PubMed: 22023932]
17. Hunter DJ, et al. Increase in bone marrow lesions associated with cartilage loss: a longitudinal magnetic resonance imaging study of knee osteoarthritis. Arthritis Rheum. 2006; 54:1529–1535. [PubMed: 16646037]
18. Dreier R. Hypertrophic differentiation of chondrocytes in osteoarthritis: the developmental aspect of degenerative joint disorders. Arthritis Res Ther. 2010; 12:216. [PubMed: 20959023]
19. Tchetina EV. Developmental mechanisms in articular cartilage degradation in osteoarthritis. Arthritis. 2011; 2011:683970. [PubMed: 22046522]
20. Blaney Davidson EN, van der Kraan PM, van den Berg WB. TGF-beta and osteoarthritis. Osteoarthritis Cartilage. 2007; 15:597–604. [PubMed: 17391995]
21. Yang X, et al. TGF-beta/Smad3 signals repress chondrocyte hypertrophic differentiation and are required for maintaining articular cartilage. J Cell Biol. 2001; 153:35–46. [PubMed: 11285272]
22. Wu Q, et al. Induction of an osteoarthritis-like phenotype and degradation of phosphorylated Smad3 by Smurf2 in transgenic mice. Arthritis Rheum. 2008; 58:3132–3144. [PubMed: 18821706]
23. Blaney Davidson EN, et al. Increase in ALK1/ALK5 ratio as a cause for elevated MMP-13 expression in osteoarthritis in humans and mice. J Immunol. 2009; 182:7937–7945. [PubMed: 19494318]
24. van der Kraan PM, Blaney Davidson EN, Blom A, van den Berg WB. TGF-beta signaling in chondrocyte terminal differentiation and osteoarthritis: modulation and integration of signaling pathways through receptor-Smads. Osteoarthritis Cartilage. 2009; 17:1539–1545. [PubMed: 19583961]
25. van der Kraan PM, Blaney Davidson EN, van den Berg WB. A role for age-related changes in TGFbeta signaling in aberrant chondrocyte differentiation and osteoarthritis. Arthritis Res Ther. 2010; 12:201. [PubMed: 20156325]
26. Scharstuhl A, et al. Inhibition of endogenous TGF-beta during experimental osteoarthritis prevents osteophyte formation and impairs cartilage repair. J Immunol. 2002; 169:507–514. [PubMed: 12077282]
27. Scharstuhl A, Vitters EL, van der Kraan PM, van den Berg WB. Reduction of osteophyte formation and synovial thickening by adenoviral overexpression of transforming growth factor beta/bone morphogenetic protein inhibitors during experimental osteoarthritis. Arthritis Rheum. 2003; 48:3442–3451. [PubMed: 14673995]
28. Tang Y, et al. TGF-beta1-induced migration of bone mesenchymal stem cells couples bone resorption with formation. Nat Med. 2009; 15:757–765. [PubMed: 19584867]
29. Hahn M, Vogel M, Pompesius-Kempa M, Delling G. Trabecular bone pattern factor--a new parameter for simple quantification of bone microarchitecture. Bone. 1992; 13:327–330. [PubMed: 1389573]
30. Pritzker KP, et al. Osteoarthritis cartilage histopathology: grading and staging. Osteoarthritis Cartilage. 2006; 14:13–29. [PubMed: 16242352]
31. Shi M, et al. Latent TGF-beta structure and activation. Nature. 2011; 474:343–349. [PubMed: 21677751]
32. Whyte MP, et al. Camurati-Engelmann disease: unique variant featuring a novel mutation in TGFbeta1 encoding transforming growth factor beta 1 and a missense change in TNFSF11 encoding RANK ligand. J Bone Miner Res. 2011; 26:920–933. [PubMed: 21541994]

33. Lotz M. Osteoarthritis year 2011 in review: biology. Osteoarthritis Cartilage. 2011; 20:192–196. [PubMed: 22179031]
34. Mendez-Ferrer S, et al. Mesenchymal and haematopoietic stem cells form a unique bone marrow niche. Nature. 2010; 466:829–834. [PubMed: 20703299]
35. Wiese C, et al. Nestin expression--a property of multi-lineage progenitor cells? Cell Mol Life Sci. 2004; 61:2510–2522. [PubMed: 15526158]
36. Kamekura S, et al. Osteoarthritis development in novel experimental mouse models induced by knee joint instability. Osteoarthritis Cartilage. 2005; 13:632–641. [PubMed: 15896985]
37. Goumans MJ, et al. Balancing the activation state of the endothelium via two distinct TGF-beta type I receptors. EMBO J. 2002; 21:1743–1753. [PubMed: 11927558]
38. Lorts A, Schwanekamp JA, Baudino TA, McNally EM, Molkentin JD. Deletion of periostin reduces muscular dystrophy and fibrosis in mice by modulating the transforming growth factor-beta pathway. Proc Natl Acad Sci U S A. 2012; 109:10978–10983. [PubMed: 22711826]
39. Edwards JR, et al. Inhibition of TGF-beta signaling by 1D11 antibody treatment increases bone mass and quality in vivo. J Bone Miner Res. 2010; 25:2419–2426. [PubMed: 20499365]
40. Ma Y, Li WZ, Guan SX, Lai XP, Chen DW. Evaluation oftetrandrine sustained release calcium alginate gel beads in vitro and in vivo. Yakugaku Zasshi. 2009; 129:851–854. [PubMed: 19571520]
41. Downs EC, Robertson NE, Riss TL, Plunkett ML. Calcium alginate beads as a slow-release system for delivering angiogenic molecules in vivo and in vitro. J Cell Physiol. 1992; 152:422–429. [PubMed: 1379248]
42. Zhang M, et al. Smad3 prevents beta-catenin degradation and facilitates beta-catenin nuclear translocation in chondrocytes. J Biol Chem. 2010; 285:8703–8710. [PubMed: 20097766]
43. Li TF, et al. Smad3-deficient chondrocytes have enhanced BMP signaling and accelerated differentiation. J Bone Miner Res. 2006; 21:4–16. [PubMed: 16355269]
44. Sekiya I, et al. Human mesenchymal stem cells in synovial fluid increase in the knee with degenerated cartilage and osteoarthritis. J Orthop Res. 2011; 30:943–949. [PubMed: 22147634]
45. Koyama N, et al. Pluripotency of mesenchymal cells derived from synovial fluid in patients with temporomandibular joint disorder. Life Sci. 2011; 89:741–747. [PubMed: 21958469]
46. Hunter DJ, et al. Bone marrow lesions from osteoarthritis knees are characterized by sclerotic bone that is less well mineralized. Arthritis Res Ther. 2009; 11:R11. [PubMed: 19171047]
47. Cunha SI, Pietras K. ALK1 as an emerging target for antiangiogenic therapy of cancer. Blood. 2011; 117:6999–7006. [PubMed: 21467543]
48. Guiducci S, et al. Bone marrow-derived mesenchymal stem cells from early diffuse systemic sclerosis exhibit a paracrine machinery and stimulate angiogenesis in vitro. Ann Rheum Dis. 2011; 70:2011–2021. [PubMed: 21821866]
49. Kasper G, et al. Mesenchymal stem cells regulate angiogenesis according to their mechanical environment. Stem Cells. 2007; 25:903–910. [PubMed: 17218399]
50. Goldring SR. Alterations in periarticular bone and cross talk between subchondral bone and articular cartilage in osteoarthritis. Ther Adv Musculoskelet Dis. 2012; 4:249–258. [PubMed: 22859924]
51. Li B, Aspden RM. Mechanical and material properties of the subchondral bone plate from the femoral head of patients with osteoarthritis or osteoporosis. Ann Rheum Dis. 1997; 56:247–254. [PubMed: 9165997]
52. Goldring SR. Role of bone in osteoarthritis pathogenesis. Med Clin North Am. 2009; 93:25–35. xv. [PubMed: 19059019]
53. Goldring MB, Goldring SR. Osteoarthritis. J Cell Physiol. 2007; 213:626–634. [PubMed: 17786965]
54. Chytil A, Magnuson MA, Wright CV, Moses HL. Conditional inactivation of the TGF-beta type II receptor using Cre:Lox. Genesis. 2002; 32:73–75. [PubMed: 11857781]
55. Qiu T, et al. TGF-beta type II receptor phosphorylates PTH receptor to integrate bone remodelling signalling. Nat Cell Biol. 2010; 12:224–234. [PubMed: 20139972]

56. Jones MD, et al. In vivo microfocal computed tomography and micro-magnetic resonance imaging evaluation of antiresorptive and antiinflammatory drugs as preventive treatments of osteoarthritis in the rat. Arthritis and rheumatism. 2010; 62:2726–2735. [PubMed: 20533290]

57. Lee JH, et al. Subchondral fluid dynamics in a model of osteoarthritis: use of dynamic contrast-enhanced magnetic resonance imaging. Osteoarthritis and cartilage / OARS, Osteoarthritis Research Society. 2009; 17:1350–1355.

58. Wu X, et al. Inhibition of Sca-1-positive skeletal stem cell recruitment by alendronate blunts the anabolic effects of parathyroid hormone on bone remodeling. Cell stem cell. 2010; 7:571–580. [PubMed: 21040899]

59. Cao X, et al. Irradiation induces bone injury by damaging bone marrow microenvironment for stem cells. Proceedings of the National Academy ofSciences of the United States of America. 2011; 108:1609–1614.

60. Angeby-Moller K, Berge OG, Hamers FP. Using the CatWalk method to assess weight-bearing and pain behaviour in walking rats with ankle joint monoarthritis induced by carrageenan: effects of morphine and rofecoxib. J Neurosci Methods. 2008; 174:1–9. [PubMed: 18634823]

61. Hamers FP, Koopmans GC, Joosten EA. CatWalk-assisted gait analysis in the assessment of spinal cord injury. J Neurotrauma. 2006; 23:537–548. [PubMed: 16629635]

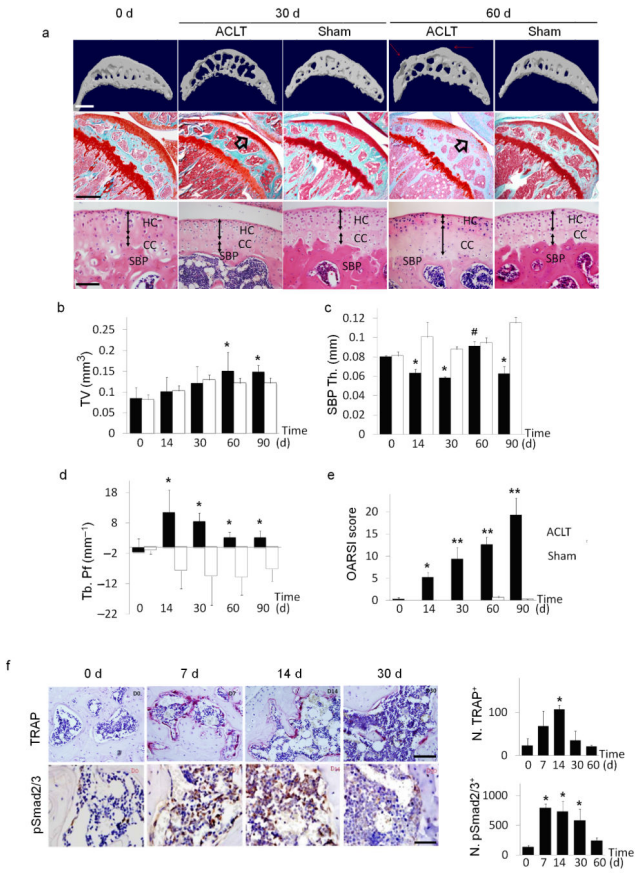


**Figure 1. Upregulated TGF–β signaling in the subchondral bone is associated with changes of subchondral bone architecture in ACLT mice**

**(a(top))** Three–dimensional high–resolution μCT images of tibial subchondral bone medial compartment (sagittal view) at 0, 30, or 60 days post sham or ACLT surgery. Altered morphology of subchondral bone plate is indicated by red arrows. Scale bar, 500 μm. **(a(center))** Sanfranin O–Fast green staining of sagittal sections of tibia medial compartment, proteoglycan (red) and bone (green). Arrows indicate loss of proteoglycan at 30 and 60 days post–surgery. Scale bar, 500 μm. **(a(bottom)** H&E staining of subchondral bone plate (SBP) and cartilage. Hyaline cartilage (HC) and calcified cartilage (CC) thickness are indicated by double arrowed lines. Scale bar, 100 μm. **(b–d)** Quantitative analysis of structural parameters of subchondral bone byμCT analysis: total tissue volume (TV), thickness of subchondral bone plates (SBP Th) and trabecular pattern factor (Tb. Pf). $n = 8$; $^{*}P < 0.05$ vs. sham group at corresponding time points; $^{\#}P < 0.05$ vs. ACLT group at 30 days post–surgery. **(e)** OARSI scores at 0–90 days post surgery. $n = 8$; $^{*}P < 0.05$ and $^{**}P < 0.01$ vs. Day 0 group. **(f)** TRAP staining (pink, top), scale bar, 200 μm and immunohistochemical analysis of pSmad2/3$^{+}$ cells (brown, bottom), scale bar, 100 μm in mouse tibial subchondral bone after ACLT surgery. Quantitative analysis of TRAP$^{+}$ or p–Smad2/3$^{+}$ cells per bone marrow area (mm$^{2}$), reported as mean ± SD. $n = 8$; $^{*}P < 0.05$ vs. Day 0 group.

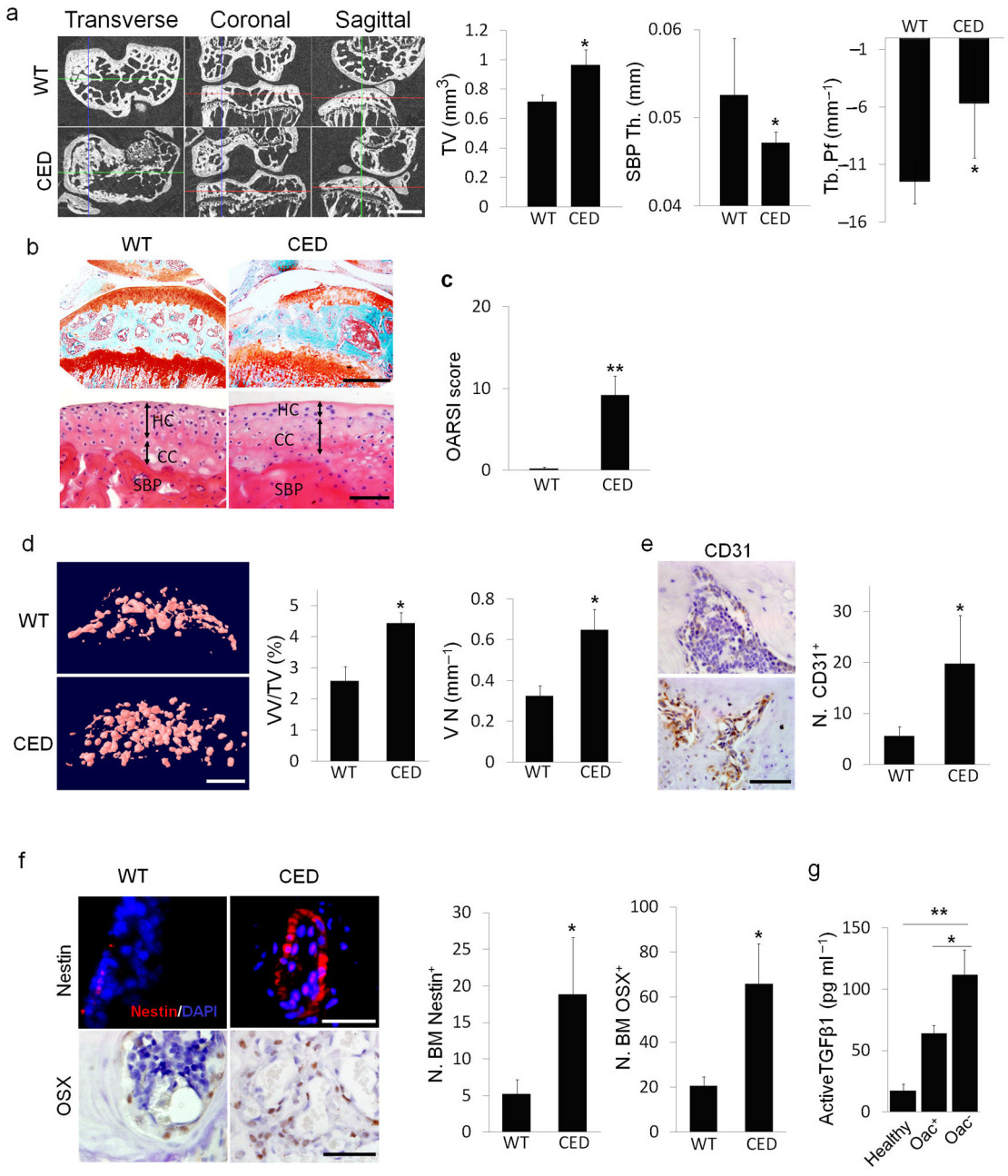


**Figure 2. CED mice with transgenic activating mutation of TGF–β1 demonstrates knee OA phenotype**

**(a)** μCT images of transverse, coronal and sagittal views of tibia subchondral bone of 4 month old CED mice vs. wild–type (WT) littermates. Scale bar, 1mm, with quantitative analysis of structural parameters of subchondral bone: total tissue volume (TV), thickness of subchondral bone plates (SBP Th) and trabecular pattern factor (Tb. Pf). **(b)** Sanfranin O–Fast green, scale bar, 500 μm**(top)** and H&E staining of sagittal sections of tibia medial compartment, scale bar, 100 μm**(bottom)**. Double arrowed lines indicate hyaline cartilage (HC) and calcified cartilage (CC) thickness. Subchondral bone plate = SBP. **(c)** OARSI

scores of CED vs. WT littermates. **(d)** CT–based micro-angiography of tibia subchondral bone of CED vs. WT littermates with quantification of vessel volume relative to tissue volume (VV/TV) and vessel number (VN). Scale bar, 500 μm. **(e,f)** Immunohistochemical or immunofluorescent analysis of $CD31^+$ (brown), scale bar, 50 μm **(e)**; $nestin^+$ (red, top), scale bar, 50 μm; $osterix^+$ (brown, bottom) cells, scale bar, 100 μm. DAPI stains nuclei (blue) **(f(top))** in tibial subchondral bone of CED vs. WT littermates. **(a–f)** $n = 10$; $^*P < 0.05$, $^{**}P < 0.01$. **(g)** ELISA analysis of active TGF–β1 in condition medium of human tibia subchondral bone specimen. Healthy: subchondral bone collected from healthy donors, $Oac^+$: OA subchondral bone with articular cartilage, $Oac^-$: OA subchondral bone without articular cartilage. $n = 10$; $^*P < 0.05$; $^{**}P < 0.01$. Data reported as mean ± SD.

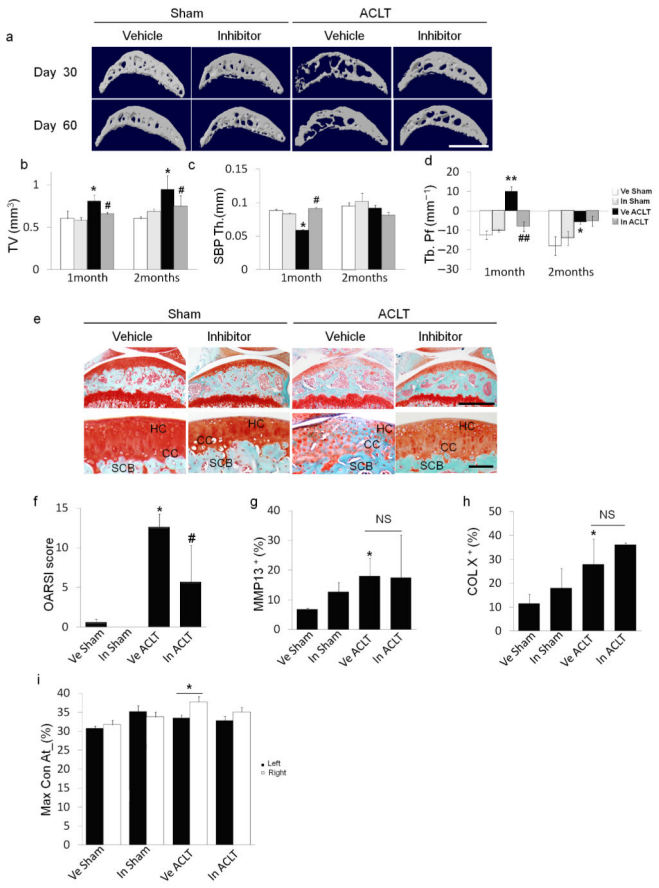


**Figure 3. TβRI inhibitor stabilized subchondral bone architecture and attenuated articular cartilage degeneration in ACLT mice**

**(a)** Three–dimensional μCT images of tibia subchondral bone medial compartment (sagittal view) of mice treated with 1 mg $kg^{-1}$ of TβRI inhibitor daily for 30 days and sacrificed 1 or 2 months post ACLT or sham surgery. Scale bar, 1 mm. **(b–d)** Quantitative analysis of structural parameters of subchondral bone by μCT analysis: tissue volume (TV), thickness of subchondral bone plate (SBP), and trabecular pattern factor (Tb. Pf). **(e)** Sanfranin O–fast green staining of articular cartilage in sagittal sections of tibia medial compartment from mice treated with vehicle or inhibitor for 1 month and sacrificed 2 months post ACLT or sham surgery. Scale bar, 500 μm **(top)** or 100 μm **(bottom)**. (f) OARSI scores of sham or ACLT mice treated with either vehicle (Ve) or TβRI inhibitor (In). **(g, h)** Quantitative analysis of the percentage of $MMP13^+$ and type X $collagen^+$ chondrocytes in immunohistochemically stained articular cartilage tissue sections. (i) Maxcontactat(%) of the gait analysis in mice 2 months post ACLT or sham surgery treated with vehicle or inhibitor for 1 month. $n$ = 8–12; $^*P < 0.05$ $^{**}P < 0.01$ vs. Ve Sham; $^{\#}P < 0.05$, $^{\#\#}P < 0.01$ vs. Ve ACLT, NS: not significant. Data reported as mean ± SD.

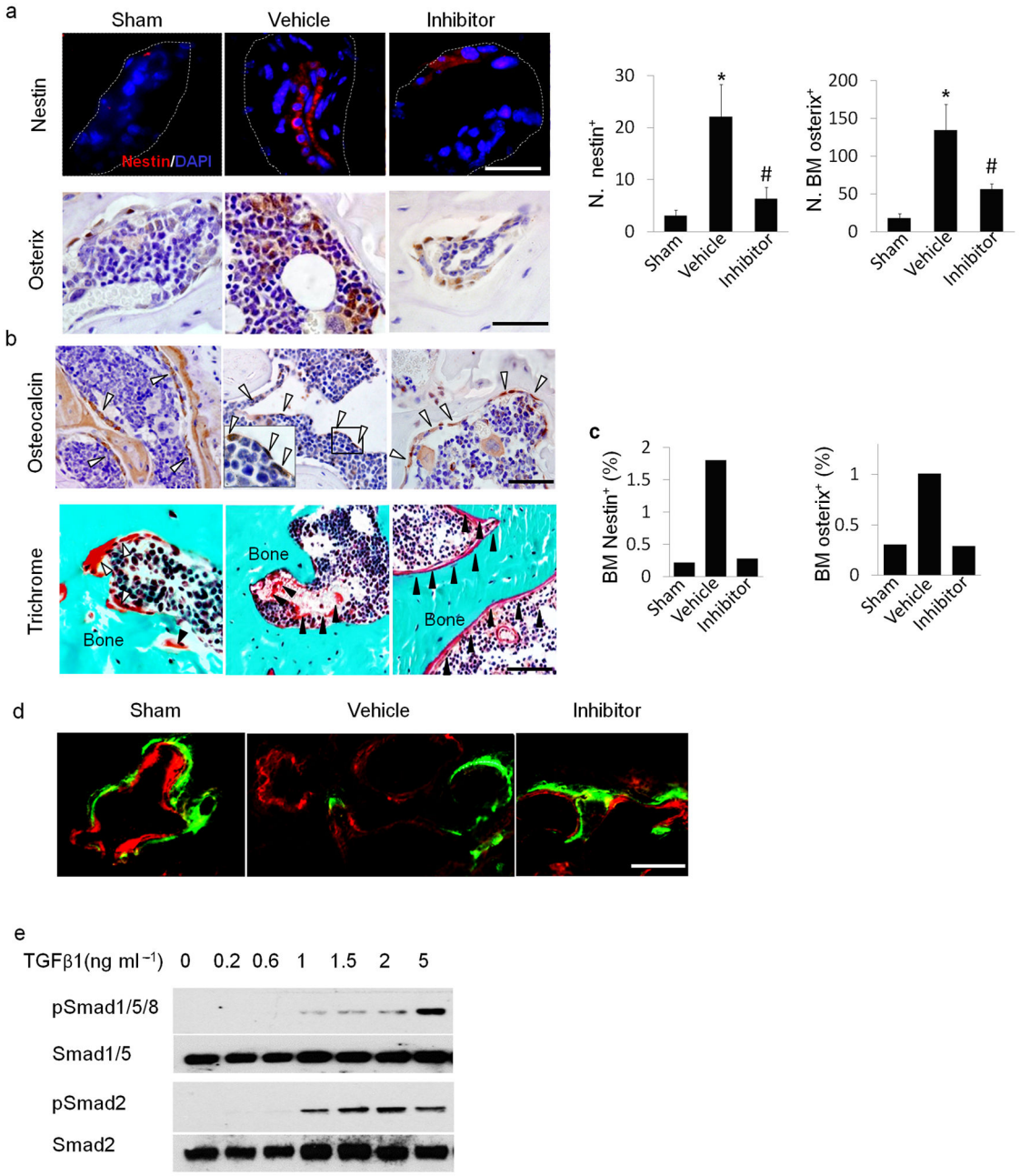

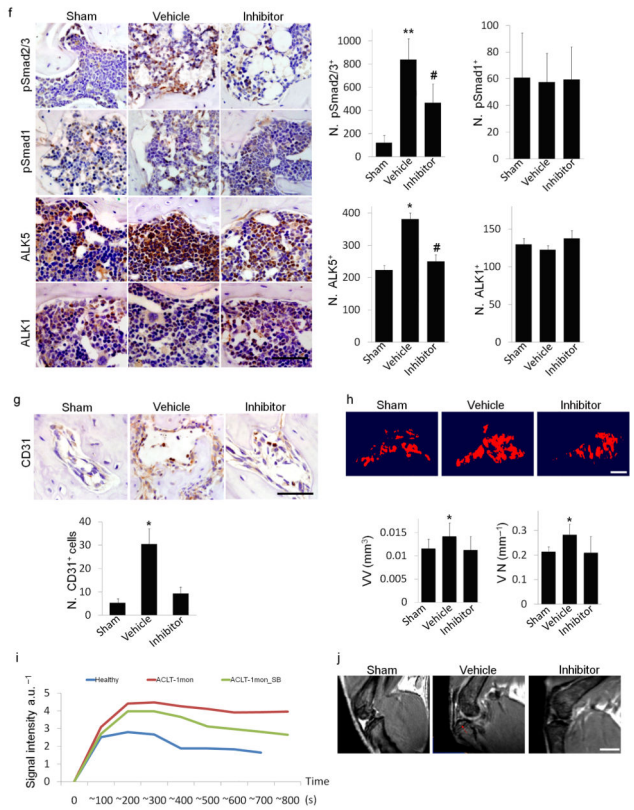


**Figure 4. TβRI inhibitor reduced uncoupled bone formation and angiogenesis in ACLT mice**

**(a)** Immunofluorescent or immunohistochemical analysis and quantification of nestin (red) and osterix (brown) in tibial subchondral bone collected one month after sham operation treated with vehicle (Sham), ACLT operated treated with vehicle (Vehicle), or ACLT operated treated with TβRI inhibitor (Inhibitor). DAPI stains nuclei (blue) **(top)**. Scale bars, 50 μm.**(b)** Immunohistochemical analysis of osteocalcin (brown) and trichrome staining in tibial subchondral bone sections. Scale bars, 50 μm. Open arrowheads indicating osteocalcin$^{+}$ cells and close arrowheads indicating osteoid. **(c)** Flow cytometry analysis of nestin and osterix in bone marrow from mouse subchondral bone. **(d)** Calcein (green) and xylenol orange (orange) fluorescent double labeling. Scale bar, 100 μm. **(e)** Western blot analysis of pSmad1/5/8, Smad1/5, pSmad2 and Smad2 of in cultured MSCs treated with increasing doses of recombinant hTGF–β1 **(f)** Immunohistochemical analysis and quantification of pSmad2/3, pSmad1, ALK5 and ALK1 (all stained brown) in subchondral bone of the mice 2 weeks post surgery. Scale bar, 50 μm. **(g)** Immunohistochemical analysis and quantification of CD31 (brown) in subchondral bone. Scale bar, 50 μm. **(h)** CT–based micro–angiography of the tibia subchondral bone and quantification of subchondral bone vessel volume (VV) and vessel number (VN), Scale bar, 500μm. **(i)** Perfusion rate obtained via T2 weighted MRI scanning with contrast. **(j)** Representative MRI T1 weighted images. Red arrow indicates bone marrow lesion. $n$ = 8–12; *$P$ < 0.05 vs. sham; $^{\#}P$ < 0.05 vs. vehicle.

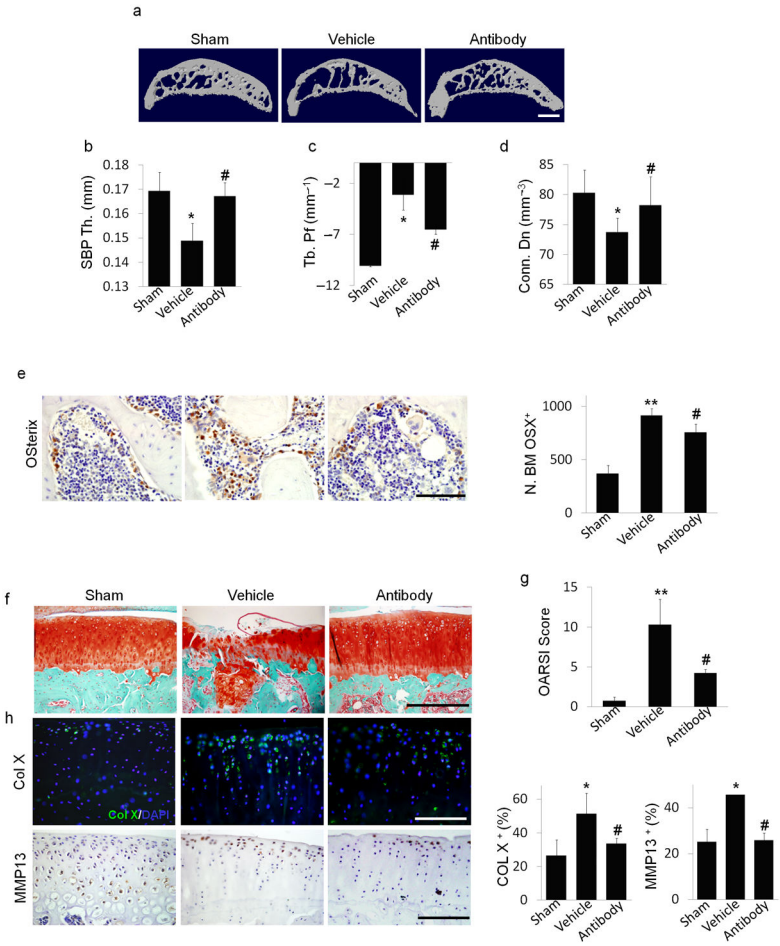


**Figure 5. Local subchondral administration of TGF–β antibody reduced abberant subchondral bone formation and articular cartilage degeneration in ACLT rats**

**(a)** Three dimensional μCT images of tibia subchondral bone medial compartment (sagittal view) in rats that underwent sham (Sham) or ACLT surgery with implantation of an alginate bead containing either vehicle (Vehicle) or TGF–β antibody (Antibody) 3 months post surgery. Scale bar, 1 mm. **(b–d)** Quantitative analysis of structural parameters of subchondral bone by μCT analysis: thickness of subchondral bone plate (SBP), trabecular pattern factor (Tb. Pf) and connectivity density (Conn. Dn). **(e)** Immunohistochemical and quantitative analysis of osterix (brown). Scale bars, 100 μm. **(f)** Sanfranin O–fast green staining of sagittal sections of subchondral tibia medial compartment, scale bar, 400 μm. **(g)** OARSI scores. **(h)** Immunofluorescent or immunohistochemical and quantitative analysis of type X collagen (green,) and MMP13 (brown) in articular cartilage. DAPI stains nuclei (blue) **(center)**. Scale bars, 200 μm. $n = 8$; $^{*}P < 0.05$, $^{**}P < 0.01$ vs. sham, $^{\#}P < 0.05$ vs. vehicle ACLT rats.

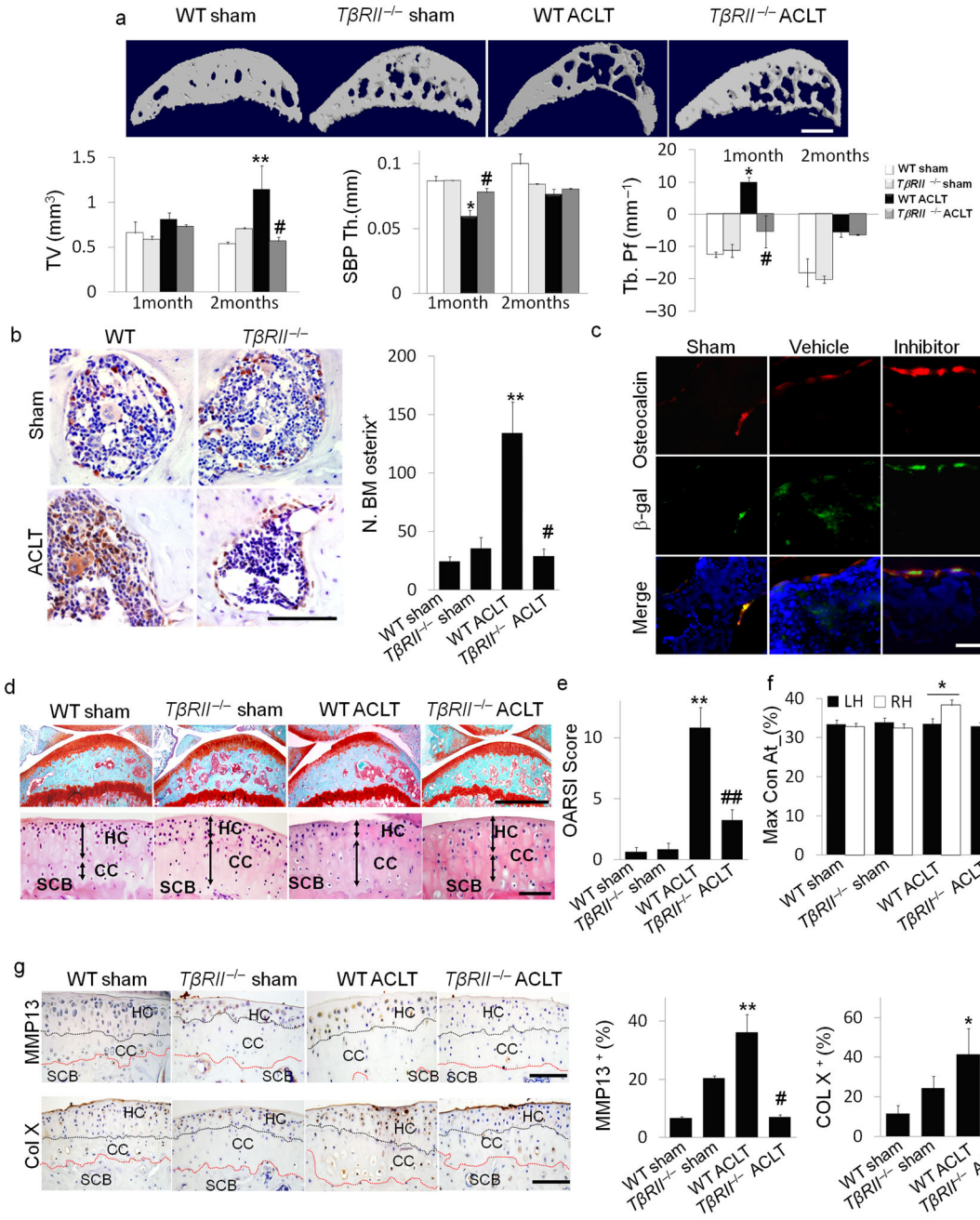

h

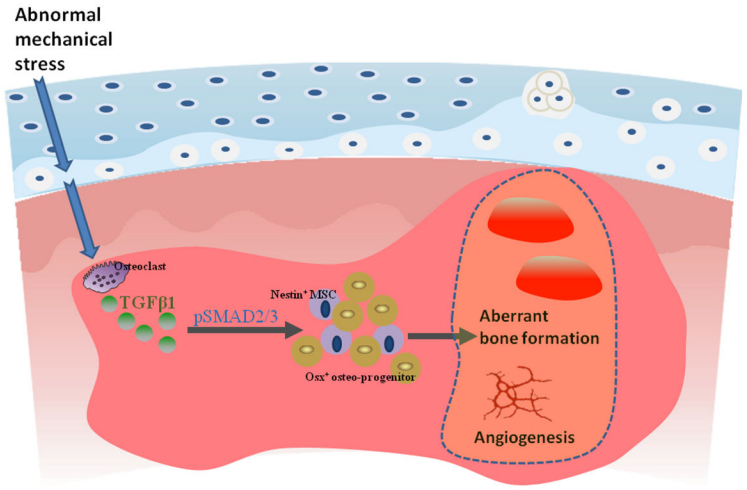


**Figure 6. Inducible knockout of *TβRII* in nestin$^{+}$ cells reduced the changes in subchondral bone and articular cartilage in ACLT mice**

**(a)** Three–dimensional μCT images of tibia subchondral bone medial compartment (sagittal view) in wild–type (WT) or *Nestin–Cre$^{TM}$ER::TβRII$^{fl/fl}$ (TβRII$^{-/-}$)* mice 2 months after undergoing sham or ACLT surgery. Scale bar, 500 μm, and quantitative analysis of structural parameters of subchondral bone by μCT analysis: subchondral bone tissue volume (TV), thickness of subchondral bone plate (SBP), and trabecular pattern factor (Tb. Pf). **(b)** Immunohistochemical and quantitative analysis of osterix (brown). Scale bar, 100 μm. **(c)** Double–immunofluorescent analysis of osteocalcin (red) and β–gal (green) in subchondral bone of *Nestin–Cre$^{TM}$ER:: Rosa26–LacZ$^{fl/fl}$* mice that underwent sham or ACLT operation and were treated with vehicle– or TβRI inhibitor. Scale bar, 40 μm. **(d)** Sanfranin O–fast green and H&E staining of the sagittal sections of tibia medial compartment. Scale bar, 100 μm. **(e)** OARSI scores. **(f)** Max_contact_at(%) of the gait analysis in mice. **(g)** Immunohistochemical and quantitative analysis of MMP13 and type X collagen (both stain brown). HC = hylane cartilage; CC = calcified cartilage; SCB = subchondral bone. $n = 8$; $^{*}P < 0.05$, $^{**}P < 0.01$ vs. wild type sham, $^{\#}P < 0.05$, $^{\#\#}P < 0.01$ vs. wild type ACLT group. Scale bars, 100 μm. **(h)** Model of elevated active TGF–β1 in the subchondral bone at the onset of OA. TGF–β1 is activated in the subchondral bone in response to abnormal mechanical loading. The accumulated high concentrations of active TGF–β1 stimulate increases in MSCs and osteoprogenitors in the marrow, which lead to aberrant bone formation and angiogenesis for OA progression.